Supplementary Information

Insights into the Intricate Charge Photoaccumulation in a Polyoxometalate–Bodipy Covalent Hybrid

Christian Cariño, Naguy Moussa, Sébastien Blanchard, Albert Solé-Daura, Anna Proust and Guillaume Izzet

Contents:

at 690 nm reflects the difference in the reactivity of the POM($2e^-$) and POM($1e^-$) towards oxidation.

11. **Figure S10.** Formation of Ph_3PO observed by ^{31}P {^1H} NMR (CD_3CN, 121 MHz) after adding 10 mM Ph_3P and passing a stream of O_2 to a solution of **1** (0.5 mM) after its irradiation in the presence of TEA (1M). The green-shaded region is the chemical shift of the POM, while the red- and purple-shaded regions are for Ph_3P and Ph_3PO, respectively.

12. **Figure S11.** Reactivity of the photoreduced compound **1** with an equivalent of various PCET reagents: benzoquinone, BQ (*top*), anthraquinone, AQ (*middle*), and TEMPO (*bottom*).

13. **Table S1.** Bond dissociation free energy (BDFE) values of the reduced forms (XH_n) of various proton-coupled electron transfer reagents (X) in MeCN (unless stated). Values were taken from ref 17

14. **Figure S12.** Combined polyhedral and balls-and-sticks representation of the model system of the Dawson-bodipy hybrid $[P_2W_{17}O_{61}\{O(SiC_{31}H_{30}N_2BF_2)_2\}]^{6-}$ used in DFT calculations. Color code: C (gray), H (white), Si (yellow), O (red), W (blue), P (green).

15. **Figure S13.** a) Molecular electrostatic potential (MEP) of the POM($1e^-$) system, represented on its B3LYP-optimized structure. Red-coloured regions indicate areas of high negative charge, while blue-coloured regions correspond to areas with low electron density. (b, c) Illustrative representations of the bridging oxygen positions in the POM structure that accommodate the first and second proton, respectively.

16. **Figure S14.** Comparison of the energy levels of POM LUMOs (lowest unoccupied molecular orbitals) calculated at the B3LYP level as function of their redox and protonation state. Note that for the open-shell POM($1e^-$) system, the LUMO energy is taken as the eigenvalue of the lowest unoccupied beta orbital within the unrestricted Kohn-Sham formalism.

17. References

1. General methods

Materials The bodipy-POM dyads $(TBA)_6[P_2W_{17}O_{61}\{O(Si\text{-}C_{31}H_{30}N_2BF_2)_2\}]$ (**1**) $(TBA)_4[PW_{11}O_{39}\{SnC_{31}H_{30}BF_2N_2\}]$ (**2**), and $(TBA)_6[P_2W_{17}O_{61}\{O(Si\text{-}C_6H_4I)_2\}]$ (**3**) were synthesized as described in literature.[1,2]

Electrochemistry. Electrochemical studies were performed with an Autolab PGSTAT 100 workstation. Analyses were carried out in dry, deaerated MeCN solutions containing 0.5 mM of **3** with 0.1 M $TBAPF_6$ and 1 M TEA under argon atmosphere. A standard three electrode cell was used with glassy carbon and a platinum wire as working and counter electrode, respectively. The potentials were measured against a nonaqueous calomel reference electrode in 1 M LiCl. The cyclic voltammetry (CV) measurements (scan rate = 100 mV/s) were obtained at different concentrations (0, 50, 100, 150, 250 mM) of AcOH and TFA.

Photoreduction experiments. All experiments were carried out in MeCN dried over molecular sieves with 0.2 mM **1** (or **2**) and 1 M TEA (or TEOA), unless stated otherwise. Before use, TEA was dried over CaH_2 and freshly distilled under N_2. The organic acid (TFA or AcOH) was added according to the desired concentration (0, 20, 60, 100 mM). The working solutions (V = 2.5 mL) were prepared in a custom-designed Schlenk flask and degassed by freeze-pump-thaw while covered with aluminum foil to prevent exposure to light.

The samples were irradiated under constant stirring with a 300-W xenon lamp (Oriel) operating at 280 W coupled with a water-filled liquid filter (Newport) and a 10CGA-385 long-pass optical filter (Newport) to eliminate IR and UV radiations, respectively. A biconvex lens was also used to focus the irradiation onto the volume of the solution. UV-visible spectra were recorded in real-time during irradiation using a fast acquisition Avantes Sensline UV-Vis-NIR spectrometer equipped with a 10-mm path length fiber-optic transmission probe (Avantes) that is directly submerged in the solution being irradiated.

Spectroelectrochemistry. Two different ways of spectroelectrochemistry were employed in the study, the first of which involves the determination of the molar absorption coefficients of the reduced forms of the Dawson POM. Bulk electrolysis on 0.1 mM of **3** in MeCN with 0.1 M $TBAPF_6$ was performed using a custom-designed cell with two compartments separating the working (liquid Hg) and reference (non-aqueous SCE) electrodes from the counter electrode (graphite). The solution was purged and kept under argon atmosphere. The $1e^-$- and $2e^-$-reduced species of **3** were successively generated by applying a potential of -0.9 and then -1.1 V. The absorbance spectra were recorded using a Hellma® quartz immersion probe of 10-mm path length.

The second approach was done to qualitatively identify the reduced POM species formed at a given potential. Here, an in-house three-electrode cell was used incorporating a fiber-optic transmission dip probe connected to a fast acquisition UV-Vis-NIR spectrophotometer. The probe was placed in front of the glassy carbon working electrode at an optimal distance determined by the probe's integration time. Analyses was performed on 0.5 mM **3** in MeCN with 1 M TEA and 0.1 M $TBAPF_6$ under continuous argon bubbling. A nonaqueous Ag/AgCl reference electrode was used along with a platinum wire counter electrode. Absorbance spectra were recorded at three-second interval simultaneous with the cyclic voltammetry

sweep (scan rate = 20 mV/s). Measurements were done at increasing quantity of TFA added (0, 50, 250 mM).

Quantum yield determination. Quantum yields were determined by adapting a previously reported procedure that employs 4,4'-dimethylazobenzene (DMAB) as a chemical actinometer that is suitable for measuring the photon flux at 532 nm generated by a monochromatic source i.e., a diode pumped solid-state laser. The photon flux was first determined by monitoring the rate of the photoisomerization of DMAB upon irradiation of its solution (50 μM) in MeCN contained in the same reaction vessel used in the photoreduction experiments. The experiment was repeated in triplicate, yielding a photon flux of 1.0×10^{-7} einstein s^{-1}. Photoreduction of **1** (0.2 mM in MeCN with 1 M TEA) was also done at various TFA concentrations using the same laser radiation source. Absorbance spectra were recorded over time with fast acquisition spectrometer to get the differential absorbance kinetics (i.e., ΔA vs time) corresponding to the formation of the POM($1e^-$) and POM($2e^-$) species.

The quantum yields, Φ, were taken as the ratio of the rate of the formation of either reduced POM species and the photon flux. It was calculated using Eq. 1 where r_i is the initial rate of formation of the POM species *i,* q_0 is the measured photon flux (einstein s^{-1}), and *V* is the solution volume (0.0025 L). Triplicate measurements were conducted at each condition.

$$\Phi = \frac{rate\ of\ formation\ of\ the\ reduced\ POM\ species,\ i}{photon\ flux} = \frac{r_i \cdot V}{q_0} \quad \text{(Eq.1)}$$

Photoluminescence measurements. Steady-state photoluminescence spectroscopy measurements were recorded with HORIBA Fluoromax® Plus using quartz cuvettes with 1-cm path length. The solutions analyzed were prepared using spectroscopic grade solvents.

The effect of acid on the emission of compound **1** was evaluated by measuring the emission intensity of a series of solutions containing 0.4 μM of **1** in MeCN with 0.04 M freshly distilled TEA and increasing quantity of trifluoroacetic acid (40, 200, 400 μM). Emission spectra (between 510-800 nm) were acquired at an excitation wavelength of 500 nm.

The fluorescence properties of **1** at different reduction states of the Dawson POM was evaluated by monitoring the emission of a completely photoreduced **1** as it spontaneously re-oxidized over time. A solution of **1** (0.1 mM) in dry MeCN containing 1 M TEA and 10 mM TFA was irradiated for about 30 minutes when the photostationary state of mostly the $2e^-$-reduced species was obtained. Emission spectra (between 510-750 nm) at an excitation wavelength of 480 nm were acquired at 5-10 min time interval. The reduction state of the POM was followed by UV-Vis absorbance spectroscopy measurements carried out at the same time.

EPR Measurements

Electron Paramagnetic Resonance (EPR) analyses: X-band EPR spectra were recorded in non-saturating conditions on a Bruker ELEXSYS 500 spectrometer at 293 K. Typical experimental conditions were: 9.396 GHz microwave frequency, 6mW microwave power, 0.1 mT modulation amplitude, 100 kHz modulation frequency. Simulations were performed using the EasySpin program.[3] Degassed solution containing 0.2 mM of **1** with 1 M TEA, 20 mM TFA and 15 mM of 5,5-dimethyl-1-pyrroline N-oxide (DMPO), the spin trap reagent, was prepared and

transferred into a cuvette for irradiation. Aliquots of the solution were collected using TLC capillary tubes, before irradiation and after 5 min of irradiation. The capillary tubes were immediately introduced in the EPR tube, previously purged with argon. The sample were kept in the dark and under inert atmosphere before and during the EPR experiment.
A degassed solution of 0.1 mM solution of 2,2,6,6-tetramethyl-piperidin-1-oxyl (TEMPO) in MeCN was measured in the same conditions as a reference to provide a semi-quantitative indication of the number of spins.

NMR. The ^{1}H (300.3 MHz) and $^{31}P\{^{1}H\}$ (121.5 MHz) were obtained at room temperature in 5 mm o.d. tubes using CD_3CN on a Bruker AvanceII 300 spectrometer equipped with a QNP probehead. NMR spectroscopic data were analysed using Bruker TopSpin® 4.1.4.

The evolution of **1** species and the by-products of its photoreduction were studied by taking the NMR spectra of de-aerated 0.5 mM **1** in CD_3CN with 1 M TEA (V = 0.5 mL) at different time points during irradiation (i.e., before irradiation, after 40 minutes of irradiation, and after 100 minutes of irradiation).

The reduction of O_2 by the photoreduced **1** was indirectly determined by adding Ph_3P and detecting the presence of Ph_3PO by $^{31}P\{^{1}H\}$ (121.5 MHz). After irradiating a de-aerated solution of 0.5 mM **1** in CD_3CN with 1 M TEA for 30 min, 100 µL of de-aerated 0.05 M Ph_3P (10 eq) was added and subsequently flushed with a stream O_2 gas. $^{31}P\{^{1}H\}$ NMR spectra were taken at different time points (i.e., before irradiation, after 30 minutes of irradiation, and after adding Ph_3P and O_2 in the dark). For comparison, a control NMR tube containing 10 mM Ph_3P under O_2 atmosphere was analysed.

Density Functional Theory (DFT) calculations were carried out at the B3LYP level of theory.[4–6] using the Gaussian 16 (rev. A.03) package.[7] For geometry optimizations and frequency calculations, metal centers (W) were described by the LANL2DZ basis set and associated pseudopotentials,[8] and supplemented with a shell of f-type polarization functions, using the exponents provided by Frenking and co-workers.[9] The remaining atoms were described by the Dunning's cc-pVDZ basis set.[10,11] Solvent effects of acetonitrile were included in both geometry optimizations and energy calculations by means of the IEF-PCM solvent model,[12] as implemented in Gaussian 16. Electronic energies were corrected by performing single-point calculations on optimized geometries using a more extended, triple-ζ quality basis set, which employed LANL2TZ(f) basis sets for metal centres and cc-pVTZ basis sets for main-group elements. A free-energy variation of +1.89 kcal mol^{-1} was applied to all species to account for the change from the reference state of 1 atm in the gas phase used in Gaussian's thermochemistry equations to the standard state of 1 M at 25 °C in solution. Free-energy barriers for Single Electron Transfer (SET) events were estimated by means of the Marcus theory,[13–15] as done successfully in previous works dealing with POM-based systems.[1,16] Our calculations focused on evaluating the energetics of processes that involve solely the POM moiety and not the bodipy antennae. Hence, the Dawson-bodipy hybrid $[P_2W_{17}O_{61}\{O(SiC_{31}H_{30}N_2BF_2)_2\}]^{6-}$ was modeled as shown in Figure S9, including only the phenyl groups directly bound to Si in the structure and capping the para positions with H capping atoms. The overall charge of -6 that the system bears is maintained in the model, as it arises from the POM group. A dataset collection of the optimized structures is available in the

ioChem-BD repository[17] and can be accessed via https://iochem-bd.iciq.es/browse/handle/100/97341.

2.

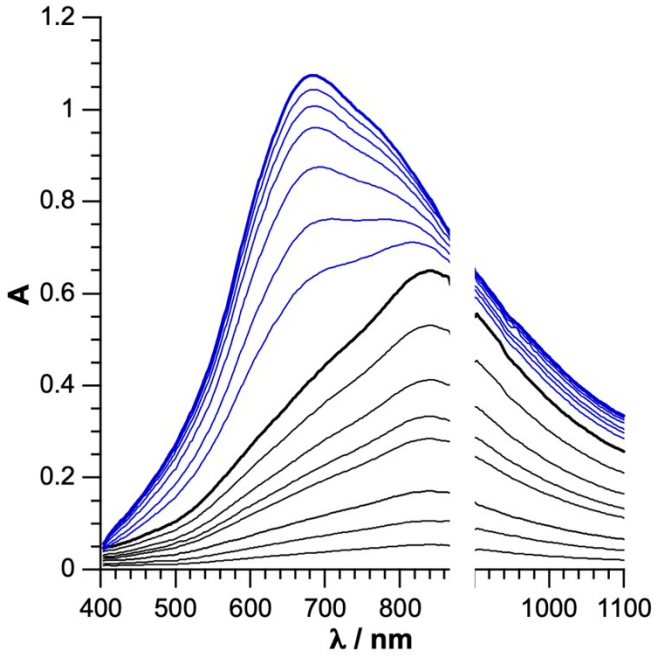

Figure S1. Spectroelectrochemical reduction of the Dawson-silyl reference compound **3** (0.1 mM) in 0.1 M $TBAPF_6$ in MeCN at -0.9 V (black) and -1.1 V(blue) vs SCE.

3.

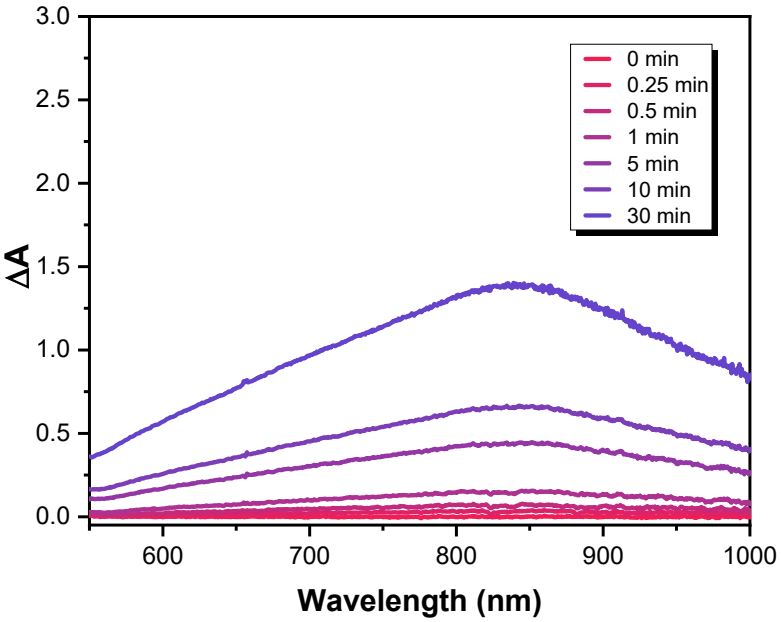

Figure S2. Evolution of the absorbance spectra upon irradiation (deaerated solution) of **1** (0.2 mM) in MeCN containing TEOA (1 M).

4.

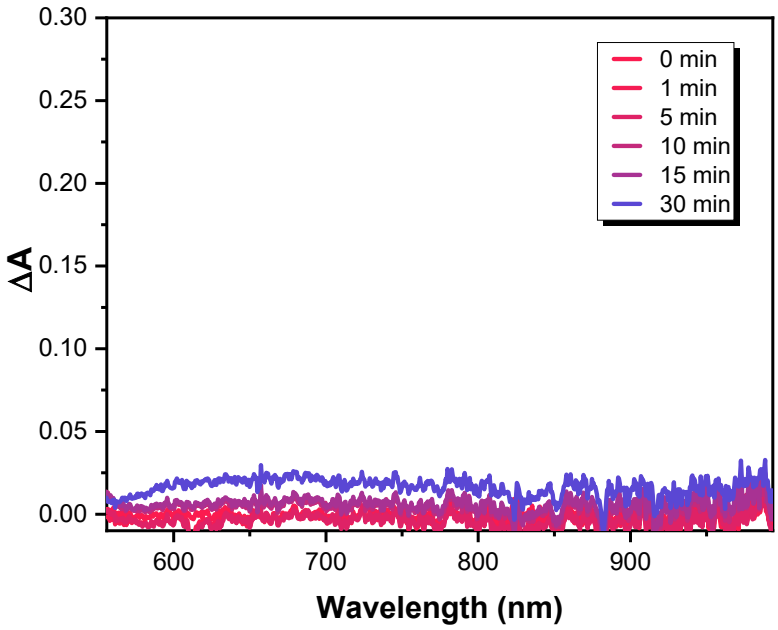

Figure S3. Evolution of the absorbance spectra upon irradiation (deaerated solution) of **2** (0.2 mM) in MeCN containing TEA (1 M).

5.

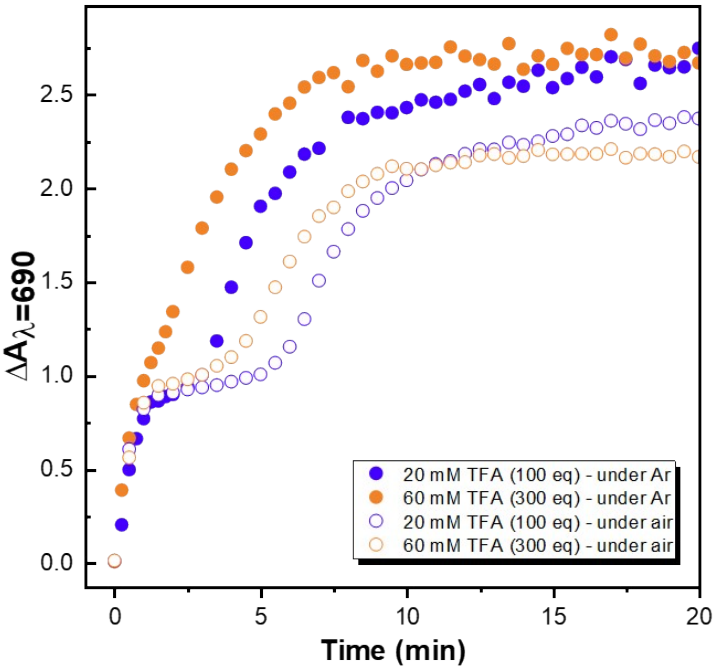

Figure S4. Comparison of the kinetics of the two-electron accumulation of 0.2 mM solution of **1** in 1M TEA in MeCN in the presence of TFA under deaerated (under Ar) and air-saturated solutions.

6.

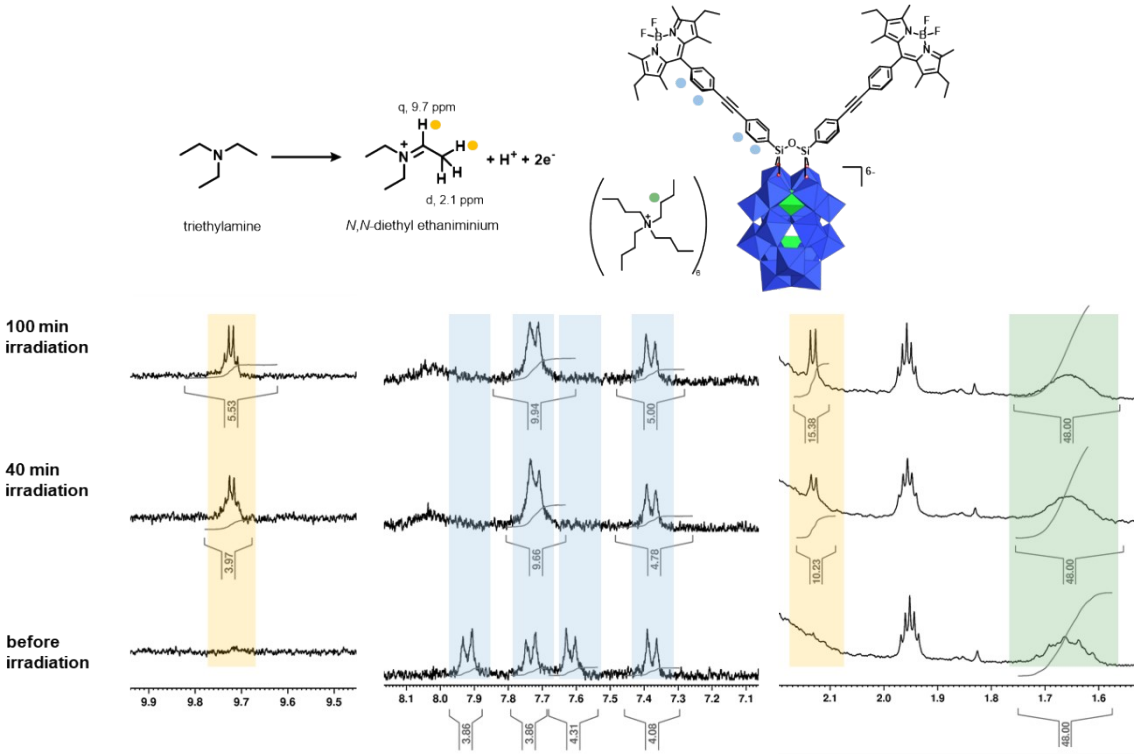

Figure S5. Evolution of the ^{1}H NMR (CD_3CN, 300 MHz) of a solution of **1** (0.5 mM) in the presence of TEA (1M) upon irradiation. The yellow-shaded region is the chemical shift for the iminium, the blue-shaded region is for the aryl of the POM hybrid, and the green-shaded region is for the TBA counterion. Integrations were calibrated relative to the protons of a methylene (δ = 1.66 ppm) of TBA.

7.

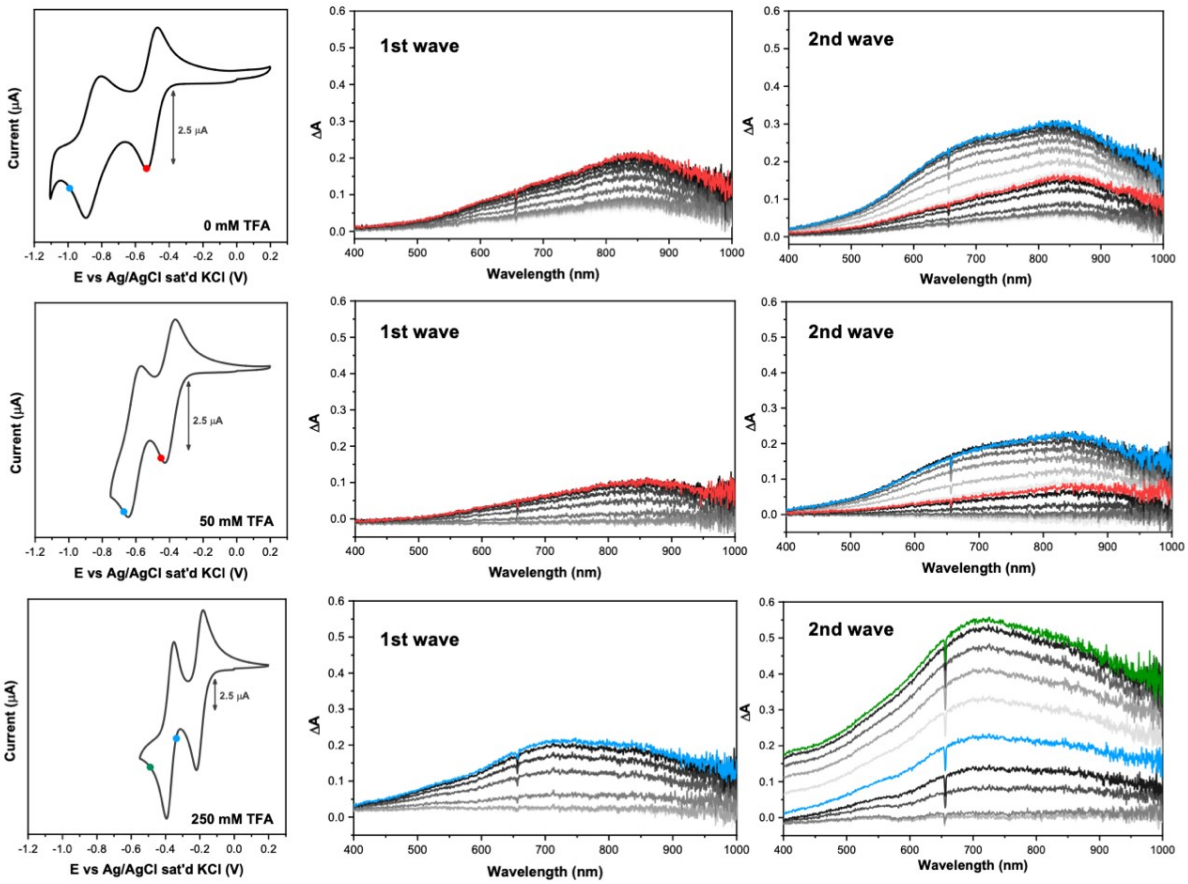

Figure S6. Spectroelectrochemistry of **3** (0.5 mM) in MeCN, 1M TEA, 0.1 M $TBAPF_6$ with 0 mM (*top*), 50 mM (*middle*), and 250 mM TFA (*bottom*). The colored line is associated with the same colored dot on the CV.

8.

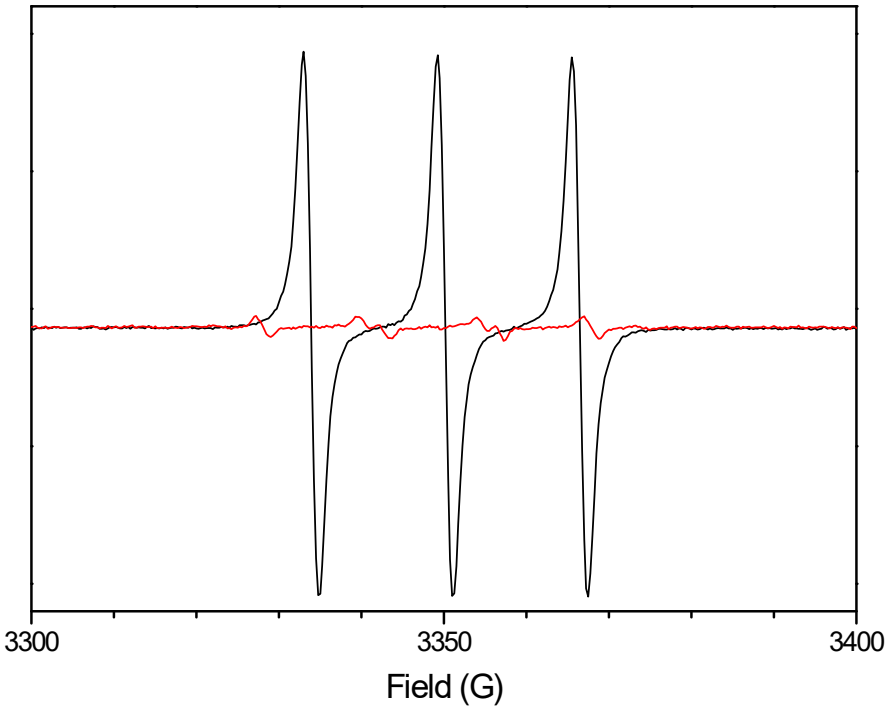

Figure S7. comparison of the X-Band EPR spectra of a 0.1 mM TEMPO solution (black curve) with that of a 0.2mM POM/ TEA (1M) / TFA (20 mM) solution irradiated for 5 min (red curve).

9.

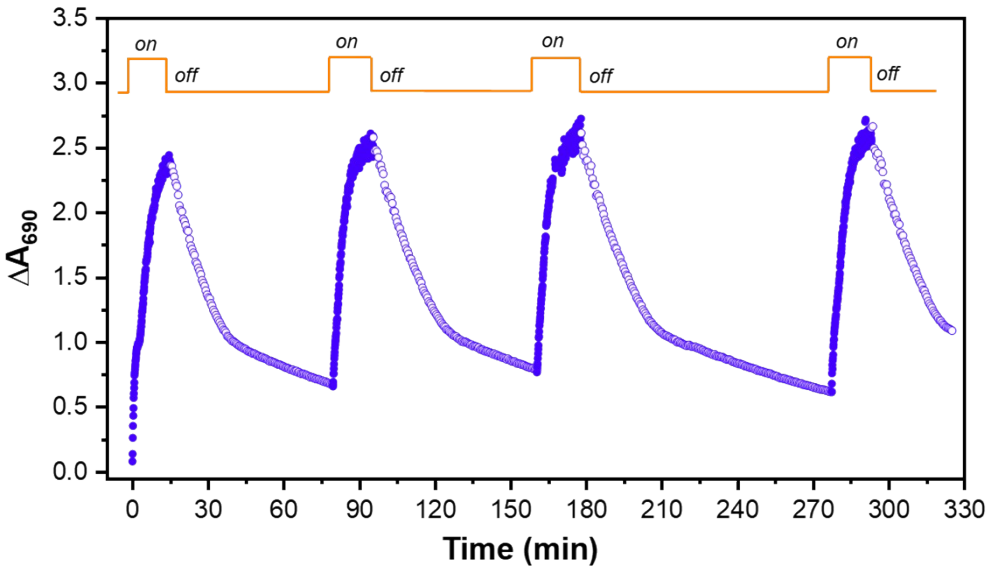

Figure S8. Evolution of the absorbance (λ = 690nm) of a deaerated solution of **1** (0.2 mM) containing 20 mM TFA and 1M TEA in MeCN upon several cycles of irradiation/dark.

10.

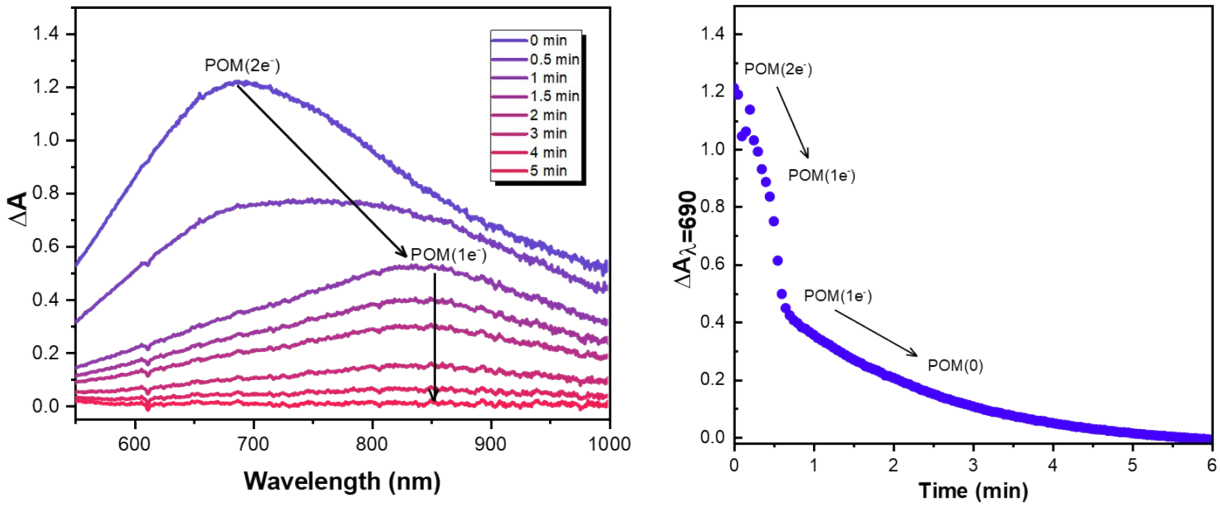

Figure S9. Evolution of the spectra (*left*) as the photoreduced **1** (0.1 mM) in 1 M TEA and 10 mM TFA re-oxidizes under a flux of O_2 gas. The kinetic plot of the absorbance at 690 nm reflects the difference in the reactivity of the POM($2e^-$) and POM($1e^-$) towards oxidation.

11.

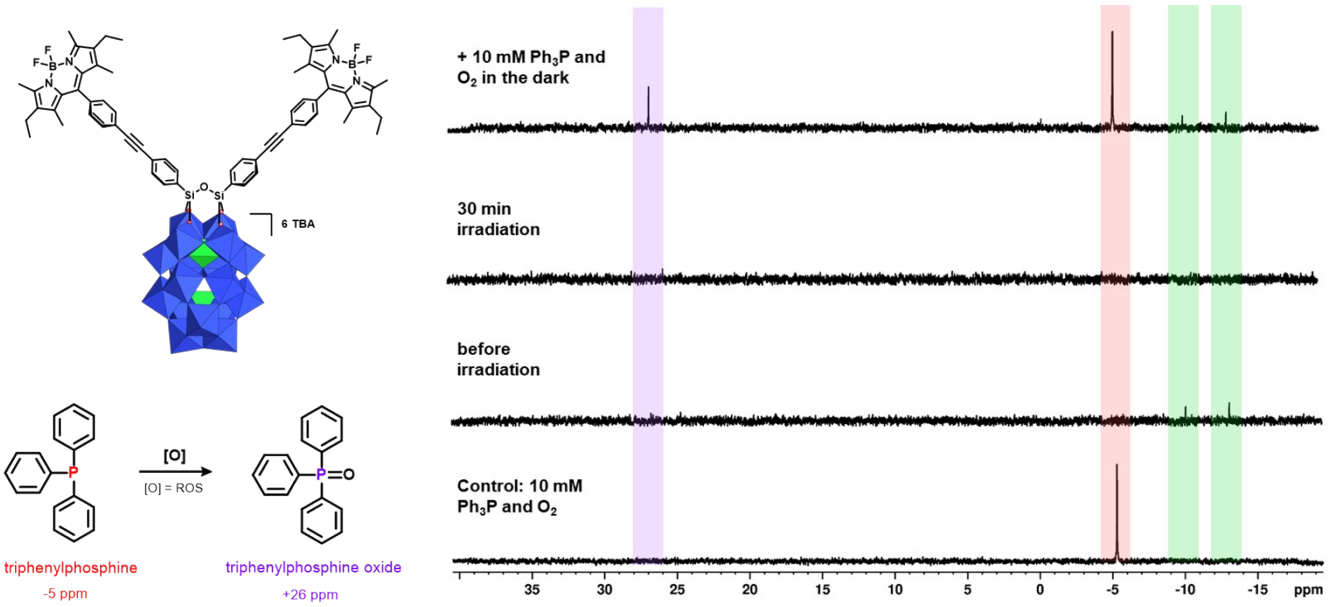

Figure S10. Formation of Ph_3PO observed by ^{31}P $\{^1H\}$ NMR (CD_3CN, 121 MHz) after adding 10 mM Ph_3P and passing a stream of O_2 to a solution of **1** (0.5 mM) after its irradiation in the presence of TEA (1M). The green-shaded region is the chemical shift of the POM, while the red- and purple-shaded regions are for Ph_3P and Ph_3PO, respectively.

12.

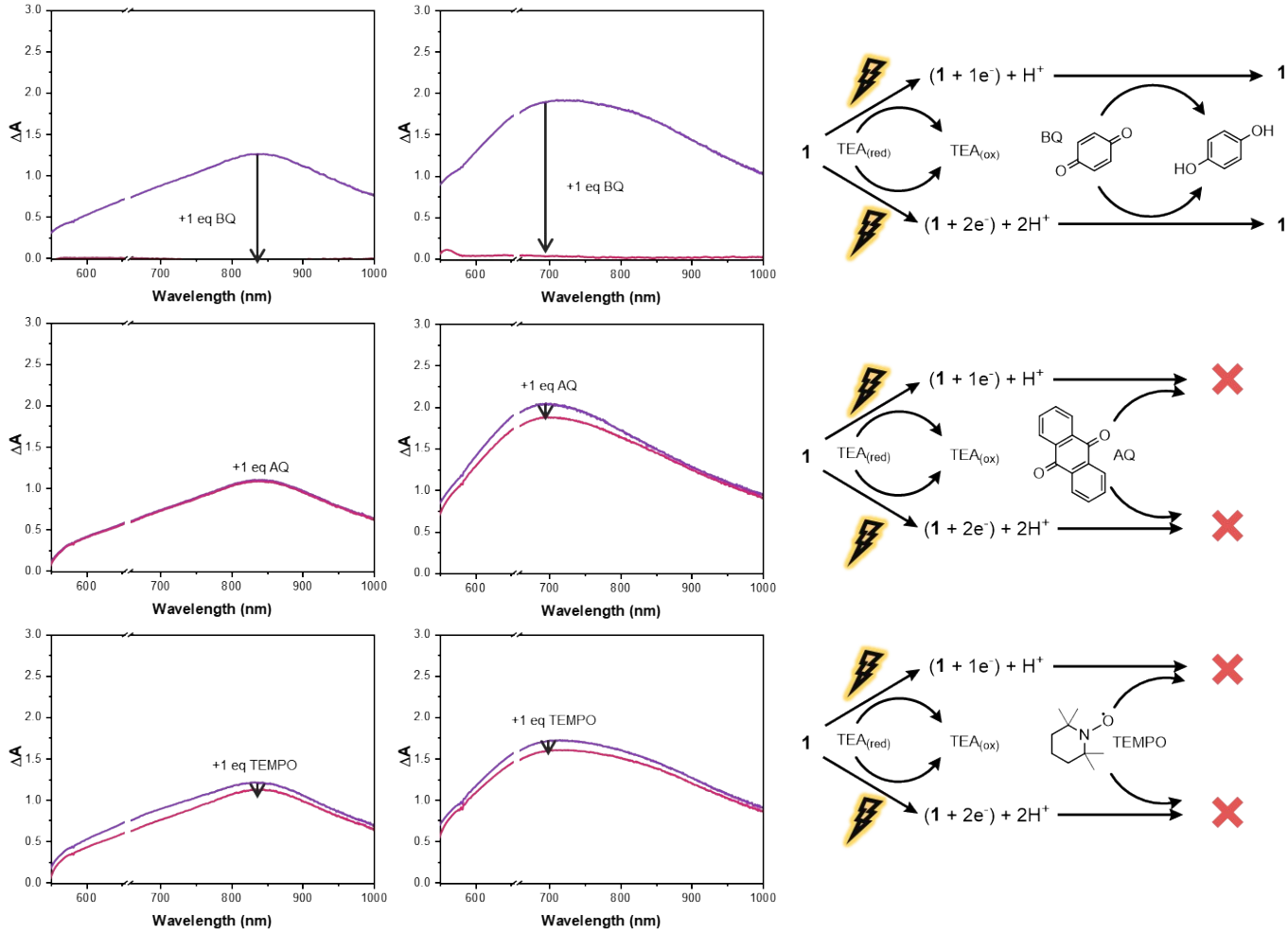

Figure S11. Reactivity of the photoreduced compound **1** with an equivalent of various PCET reagents: benzoquinone, BQ (*top*), anthraquinone, AQ (*middle*), and TEMPO (*bottom*).

13.

Table S1. Bond dissociation free energy (BDFE) values of the reduced forms (XH_n) of various proton-coupled electron transfer reagents (X) in MeCN (unless stated otherwise). Values were

substrate, X	XH_n	XH_n BDFE (kcal mol^{-1})
anthraquinone	9,10-dihydroxyanthracene	54.9 (in H_2O)
phenazine	5,10-dihydrophenazine	58.7
azobenzene	1,2-diphenylhydrazine	60.9
TEMPO	TEMPOH	66
1,4-benzoquinone	1,4-hydroquinone	67.3

taken from ref [18].

14.

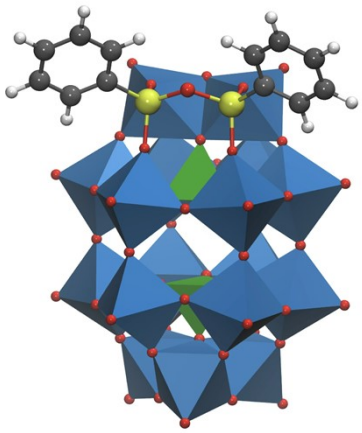

Figure S12. Combined polyhedral and balls-and-sticks representation of the model system of the Dawson-bodipy hybrid $[P_2W_{17}O_{61}\{O(SiC_{31}H_{30}N_2BF_2)_2\}]^{6-}$ used in DFT calculations. Color code: C (gray), H (white), Si (yellow), O (red), W (blue), P (green).

15.

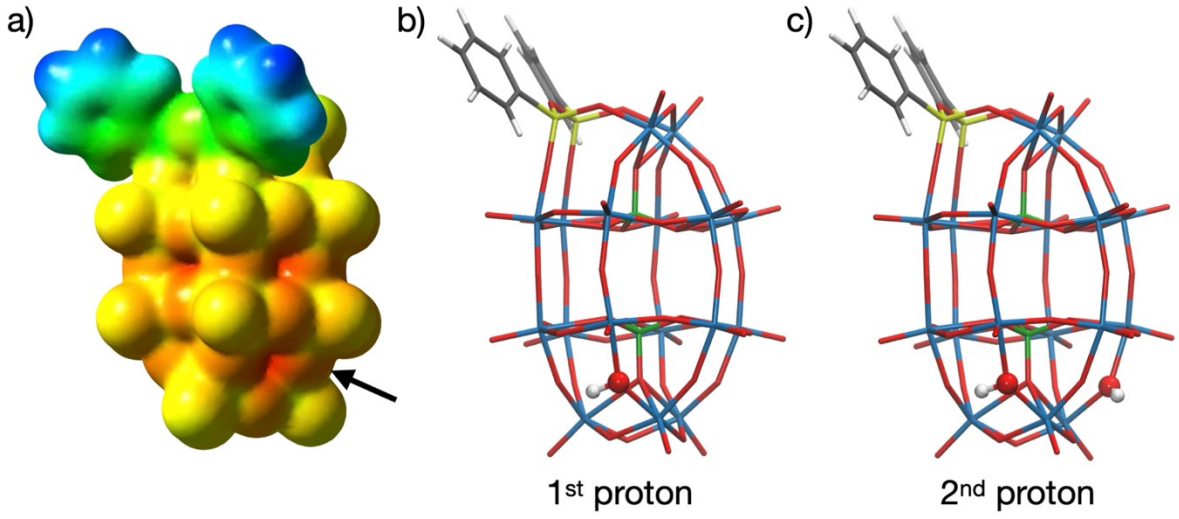

Figure S13. a) Molecular electrostatic potential (MEP) of the POM($1e^-$) system, represented on its B3LYP-optimized structure. Red-coloured regions indicate areas of high negative charge, while blue-coloured regions correspond to areas with low electron density. (b, c) Illustrative representations of the bridging oxygen positions in the POM structure that accommodate the first and second proton, respectively.

16.

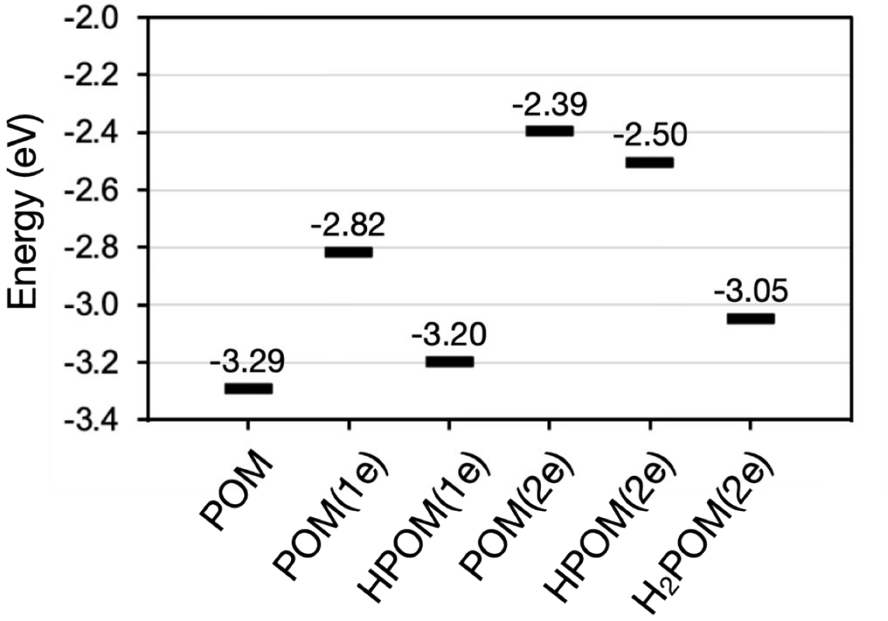

Figure S14. Comparison of the energy levels of POM LUMOs (lowest unoccupied molecular orbitals) calculated at the B3LYP level as function of their redox and protonation state. Note that for the open-shell POM($1e^-$) system, the LUMO energy is taken as the eigenvalue of the lowest unoccupied beta orbital within the unrestricted Kohn-Sham formalism.

17. References

1 G. Toupalas, J. Karlsson, F. A. Black, A. Masip-Sanchez, X. Lopez, Y. Ben M'Barek, S. Blanchard, A. Proust, S. Alves, P. Chabera, I. P. Clark, T. Pullerits, J. M. Poblet, E. A. Gibson and G. Izzet, *Angew. Chem.-Int. Ed.*, 2021, **60**, 6518–6525.

2 E. Benazzi, J. Karlsson, Y. Ben M'Barek, P. Chabera, S. Blanchard, S. Alves, A. Proust, T. Pullerits, G. Izzet and E. A. Gibson, *Inorg. Chem. Front.*, 2021, **8**, 1610–1618.

3 S. Stoll and A. Schweiger, *J. Magn. Reson.*, 2006, **178**, 42–55.

4 C. Lee, W. Yang and R. G. Parr, *Phys. Rev. B*, 1988, **37**, 785.

5 A. D. Becke, *J. Phys. Chem.*, 1993, **98**, 5648–5652.

6 P. J. Stephens, F. J. Devlin, C. F. Chabalowski and M. J. Frisch, *J. Phys. Chem.*, 1994, **98**, 11623–11627.

7 Gaussian 16, Revision A.03, Frisch, M. J.; Trucks, G. W.; Schlegel, H. B.; Scuseria, G. E.; Robb, M. A.; Cheeseman, J. R.; Scalmani, G.; Barone, V.; Petersson, G. A.; Nakatsuji, H.; Li, X.; Caricato, M.; Marenich, A. V.; Bloino, J.; Janesko, B. G.; Gomperts, R.; Mennucci, B.; Hratchian, H. P.; Ortiz, J. V.; Izmaylov, A. F.; Sonnenberg, J. L.; Williams-Young, D.; Ding, F.; Lipparini, F.; Egidi, F.; Goings, J.; Peng, B.; Petrone, A.; Henderson, T.; Ranasinghe, D.; Zakrzewski, V. G.; Gao, J.; Rega, N.; Zheng, G.; Liang, W.; Hada, M.; Ehara, M.; Toyota, K.; Fukuda, R.; Hasegawa, J.; Ishida, M.; Nakajima, T.; Honda, Y.; Kitao, O.; Nakai, H.; Vreven, T.; Throssell, K.; Montgomery, J. A., Jr.; Peralta, J. E.; Ogliaro, F.; Bearpark, M. J.; Heyd, J. J.; Brothers, E. N.; Kudin, K. N.; Staroverov, V. N.; Keith, T. A.; Kobayashi, R.; Normand, J.; Raghavachari, K.; Rendell, A. P.; Burant, J. C.; Iyengar, S. S.; Tomasi, J.; Cossi, M.; Millam, J. M.; Klene, M.; Adamo, C.; Cammi, R.; Ochterski, J. W.; Martin, R. L.; Morokuma, K.; Farkas, O.; Foresman, J. B.; Fox, D. J. Gaussian, Inc., Wallingford CT, 2016.

8 P. J. Hay and W. R. Wadt, *J. Chem. Phys.*, 1985, **82**, 270–283.

9 A. W. Ehlers, M. Böhme, S. Dapprich, A. Gobbi, A. Höllwarth, V. Jonas, K. F. Köhler, R. Stegmann, A. Veldkamp and G. Frenking, *Chem. Phys. Lett.*, 1993, **208**, 111–114.

10 T. H. Dunning Jr., *J. Chem. Phys.*, 1989, **90**, 1007–1023.

11 R. A. Kendall, T. H. Dunning Jr. and R. J. Harrison, *J. Chem. Phys.*, 1992, **96**, 6796–6806.

12 E. Cancès, B. Mennucci and J. Tomasi, *J. Phys. Chem.*, 1997, **107**, 3032–3041.

13 R. A. Marcus, *J Chem Phys*, 1956, **24**, 966–978.

14 R. A. Marcus, *J. Phys. Chem.*, 1963, **67**, 853–857.

15 R. A. Marcus, *Angew. Chem. Int. Ed.*, 1993, **32**, 1111–1121.

16 A. Solé-Daura, Y. Benseghir, M.-H. Ha-Thi, M. Fontecave, P. Mialane, A. Dolbecq and C. Mellot-Draznieks, *ACS Catal.*, 2022, **12**, 9244–9255.

17 M. Alvarez-Moreno, C. de Graaf, N. Lopez, F. Maseras, J. M. Poblet and C. Bo, *J. Chem. Inf. Model.*, 2015, **55**, 95–103.

18 C. F. Wise, R. G. Agarwal and J. M. Mayer, *J. Am. Chem. Soc.*, 2020, **142**, 10681–10691.